







## Article

# Crystal Structure and Concentration-Driven Phase Transitions in $\text{Lu}_{(1-x)}\text{Sc}_x\text{FeO}_3$ ( $0 \leq x \leq 1$ ) Prepared by the Sol–Gel Method

Andrius Pakalniškis <sup>1,\*</sup>, Denis O. Alikin <sup>2,3</sup>, Anton P. Turygin <sup>2</sup>, Alexander L. Zhaludkevich <sup>4</sup>, Maxim V. Silibin <sup>5,6</sup>, Dmitry V. Zhaludkevich <sup>4</sup>, Gediminas Niaura <sup>7</sup>, Aleksej Zarkov <sup>1,\*</sup>, Ramūnas Skaudžius <sup>1</sup>, Dmitry V. Karpinsky <sup>4,8</sup> and Aivaras Kareiva <sup>1</sup>

- <sup>1</sup> Institute of Chemistry, Vilnius University, Naugarduko 24, LT-03225 Vilnius, Lithuania; ramunas.skaudzius@chgf.vu.lt (R.S.); aivaras.kareiva@chgf.vu.lt (A.K.)
- <sup>2</sup> School of Natural Sciences and Mathematics, Ural Federal University, 620000 Ekaterinburg, Russia; denis.alikin@ua.pt (D.O.A.); anton.turygin@urfu.ru (A.P.T.)
- <sup>3</sup> Department of Physics & CICECO—Aveiro Institute of Materials, University of Aveiro, 3810-193 Aveiro, Portugal
- <sup>4</sup> Scientific-Practical Materials Research Centre of NAS of Belarus, 220072 Minsk, Belarus; zheludkevich27@gmail.com (A.L.Z.); geludkevichdima@mail.ru (D.V.Z.); dmitry.karpinsky@gmail.com (D.V.K.)
- <sup>5</sup> Institute of Advanced Materials and Technologies, National Research University of Electronic Technology “MIET”, 124498 Moscow, Russia; sil\_m@mail.ru
- <sup>6</sup> Institute for Bionic Technologies and Engineering, I.M. Sechenov First Moscow State Medical University, 119991 Moscow, Russia
- <sup>7</sup> Department of Organic Chemistry, Center for Physical Sciences and Technology (FTMC), Sauletekio Ave. 3, LT-10257 Vilnius, Lithuania; gediminas.niaura@ftmc.lt
- <sup>8</sup> Department of Materials Science and Physical Chemistry of Materials, South Ural State University, Av. Lenina, 76, 454080 Chelyabinsk, Russia
- \* Correspondence: andrius.pakalniskis@chgf.vu.lt (A.P.); aleksej.zarkov@chf.vu.lt (A.Z.)



**Citation:** Pakalniškis, A.; Alikin, D.O.; Turygin, A.P.; Zhaludkevich, A.L.; Silibin, M.V.; Zhaludkevich, D.V.; Niaura, G.; Zarkov, A.; Skaudžius, R.; Karpinsky, D.V.; et al. Crystal Structure and Concentration-Driven Phase Transitions in  $\text{Lu}_{(1-x)}\text{Sc}_x\text{FeO}_3$  ( $0 \leq x \leq 1$ ) Prepared by the Sol–Gel Method. *Materials* **2022**, *15*, 1048. <https://doi.org/10.3390/ma15031048>

Academic Editor: Chao Xu

Received: 28 December 2021

Accepted: 28 January 2022

Published: 29 January 2022

**Publisher’s Note:** MDPI stays neutral with regard to jurisdictional claims in published maps and institutional affiliations.



**Copyright:** © 2022 by the authors. Licensee MDPI, Basel, Switzerland. This article is an open access article distributed under the terms and conditions of the Creative Commons Attribution (CC BY) license (<https://creativecommons.org/licenses/by/4.0/>).

**Abstract:** The structural state and crystal structure of  $\text{Lu}_{(1-x)}\text{Sc}_x\text{FeO}_3$  ( $0 \leq x \leq 1$ ) compounds prepared by a chemical route based on a modified sol–gel method were investigated using X-ray diffraction, Raman spectroscopy, as well as scanning electron microscopy. It was observed that chemical doping with Sc ions led to a structural phase transition from the orthorhombic structure to the hexagonal structure via a wide two-phase concentration region of  $0.1 < x < 0.45$ . An increase in scandium content above 80 mole% led to the stabilization of the non-perovskite bixbyite phase specific for the compound  $\text{ScFeO}_3$ . The concentration stability of the different structural phases, as well as grain morphology, were studied depending on the chemical composition and synthesis conditions. Based on the data obtained for the analyzed samples, a composition-dependent phase diagram was constructed.

**Keywords:** phase transitions; structural phase stability;  $\text{LuFeO}_3$ ; X-ray diffraction; solid solutions

## 1. Introduction

The crystal structure and properties of compounds with perovskite structure (nominal chemical formula  $\text{ABO}_3$ ) [1–4] can be drastically modified by a chemical substitution in A- and/or B-perovskite sublattices. The introduction of elements of different ionic radii leads to the stabilization of diverse types of structural distortion described by the Goldschmidt tolerance factor [5–7]. The possibility to control physical properties via chemical doping is particularly important in regard to the formation of both electrical and magnetic orderings in these compounds, which are commonly referred to as multiferroics [8,9]. These conditions are often contradictory, since magnetic ordering usually requires partially filled d orbitals, whereas electrical ordering requires empty d orbitals of the ions occupying the B-perovskite position. However, nowadays different mechanisms allowing ferroelectricity

have been discovered (lone pair, charge ordering, geometric, and spin-driven) that permit the coexistence of both types of ordering [9,10]. The formation of efficient multiferroic compounds allows controlling their electric properties by a magnetic field and vice versa, making these compounds potentially useful for various practical applications [8,11–13].

Probably, BiFeO<sub>3</sub> is the most investigated and common multiferroic compound; however, this compound suffers from a large leakage current and is difficult to prepare. Therefore, alternatives are needed [14]. Recently, a new family of room-temperature multiferroic compounds based on LuFeO<sub>3</sub> with hexagonal structure (space group *P6<sub>3</sub>cm*) has been discovered [15,16]. It was found that LuFeO<sub>3</sub> in the hexagonal state has both ferroelectric and weak ferromagnetic ordering [17–19]. Furthermore, it has been reported that the compound in orthorhombic phase (space group *Pnma*) is antiferromagnetic below 620 K, while being in hexagonal structure, the magnetic transition shifts down to 440 K, and below 130 K, the compound has weak ferromagnetism, due to canting towards the c-axis, with the polarization being retained up to 1050 K, at least in the case of thin films [18,20]. The crystal structure and the origin of multiferroicity are similar to those specific for hexagonal manganites (e.g., YMnO<sub>3</sub>) [21].

It should be noted that the preparation of hexagonal compounds is quite difficult, and the crystal structure can be realized either using chemical substitution or in the form of thin films, as lattice is unstable under external stimuli and tends to form an orthorhombic structure specific for orthoferrites [22–25]. Due to the aforementioned unstable nature of the lattice and the difficulty of preparation and characterization of the hexagonal variant of LuFeO<sub>3</sub>, the main available results regard thin films [16–18]. However, when analyzing thin films, it is important to take into account the effect of strain and interface interactions, as they can significantly affect thin films' chemical and physical properties [15,21]. Thus, in order to fully analyze the system, it is important to perform the experiments on bulk samples of pure chemical composition. Recently, it has been shown that it is possible to stabilize the hexagonal structure of LuFeO<sub>3</sub> using chemical doping of Lu ions by other ions with similar ionic radii (e.g., Sc, Yb, Ho) using solid-state methods [26,27]. Additionally, similar structural changes can be induced by changing the cation in B position; in this case, Fe<sup>3+</sup> can be substituted with another transition metal ion, e.g., Ni and Mn [28,29]. Alternatively, the crystal structure of the parent compound can be affected by the formation of LuFeO<sub>3</sub>-based compounds using doping either by other perovskite compounds, e.g., YMnO<sub>3</sub> [30], or via diffusion into the perovskite matrix of pure iron [31].

However, there is contradictory information in the literature [26,27,29] describing the crystal structure of these compounds and their structural stability under internal (grain size, morphology, local stresses, synthesis conditions, etc.) and external (temperature, pressure, electric, and magnetic fields) stimuli. Thus, additional and detailed investigations are required. On the other hand, recently, ferroelectricity was demonstrated in single crystals of LuFeO<sub>3</sub> doped by Sc, which makes Sc a promising candidate to prepare bulk ferroelectric polycrystalline samples with interesting potential applications [32].

Taking the mentioned arguments into account, in this paper, we provide a new route to prepare Sc-doped LuFeO<sub>3</sub> polycrystalline compounds using an aqueous sol–gel synthesis procedure and provide clarification of the concentration ranges of the different structural phases present in the system and analyzed by means of SEM, EDX/EDS, X-ray diffraction, and Raman spectroscopy. The obtained results allowed determining the evolution of crystal symmetry, structural parameters, and crystalline morphology depending on the annealing conditions using the mentioned preparation method as well as analyzing this information in relation to the available structural data. Furthermore, a relation between phase formation and particle morphology was also established.

## 2. Materials and Methods

Lu<sub>2</sub>O<sub>3</sub> (99.99%, Sigma Aldrich, St. Louis, MO, USA), Sc<sub>2</sub>O<sub>3</sub> (99.9%, Sigma Aldrich), Fe(NO<sub>3</sub>)<sub>3</sub>·9H<sub>2</sub>O (98%, Alfa Aesar, Haverhill, MA, USA), ethylene glycol (EG, Lach-ner, Neratovice, Czechia), and concentrated HNO<sub>3</sub> (Lach-ner) were used as precursors. Samples

containing 0, 0.15, 0.25, 0.50, 0.75, 0.80, and 1 Sc were prepared. For the preparation of the samples, ethylene glycol-assisted sol–gel synthesis was used, obtaining for each nominal synthesis, about 1 g of the final product. Initially,  $\text{Sc}_2\text{O}_3$  was dissolved in 25 mL of  $\text{HNO}_3$  at around 100 °C (temperature of the magnetic stirrer) in a covered chemical glass under constant magnetic stirring. This was followed by the addition of  $\text{Lu}_2\text{O}_3$ , which was also dissolved in the solution. After both oxides had dissolved, nitric acid was evaporated, and the remaining liquid was washed with distilled water and finally diluted to a volume of 50 mL. Subsequently, iron nitrate was added, and the obtained solution was stirred for 1 h at around 80 °C. Then, ethylene glycol was added in a ratio of 1:1 to metal cations, and the solution was further stirred for 1 h to obtain a homogeneous solution. Finally, the solution was evaporated at 200 °C, until a gel was obtained, which was dried overnight in a furnace at 150 °C. The obtained xerogel was ground in an agate mortar and calcinated at the temperatures of 500, 650, 800, 950, 1100 °C for 1.5 h with a heating rate of 1 °C/min. Samples calcinated at 1100 °C (with 0.00, 0.25, 0.50, 0.75, 1.00 of Sc) were further sintered at 1300 and 1500 °C for 3 h at a heating rate of 5 °C/min.

XRD measurements were performed using a Rigaku MiniFlex II diffractometer using  $\text{Cu K}\alpha$  radiation ( $\lambda = 1.5418 \text{ \AA}$ ) in  $2\theta$  range from 10° to 80° with a scan speed of 5°/min and 0.02° step size. The measurement current was set to 15 mA, and the voltage was set to 30 kV. Structural Rietveld refinement was performed using FullProf software [33]. The dual-beam system FE-SEM-FIB Helios Nanolab 650 with an energy-dispersive X-ray (EDX) spectrometer INCA Energy 350 with an X-Max 20 SDD detector was employed for the measurement of chemical composition as well as for the preparation of SEM micrographs. Raman scattering measurements were conducted using an inVia Raman (Renishaw, United Kingdom) spectrometer equipped with a thermoelectrically cooled (−70 °C) CCD camera and a microscope. Raman spectra were obtained by excitation with a 532 nm beam from the CW diode-pumped solid-state (DPSS) laser (Renishaw, UK). To avoid damage of the sample, the laser power at the sample was restricted to a very low value, 0.06 mW. A 20×/0.40 NA objective lens and 1800 lines/mm grating were used during all measurements. The overall integration time was 800 s. The position of the Raman bands on the wavenumber axis was calibrated by the polystyrene film standard spectrum. The parameters of the bands were determined by fitting the experimental spectra with Gaussian–Lorentzian shape components using GRAMS/A1 8.0 (Thermo Scientific, Waltham, MA, USA) software.

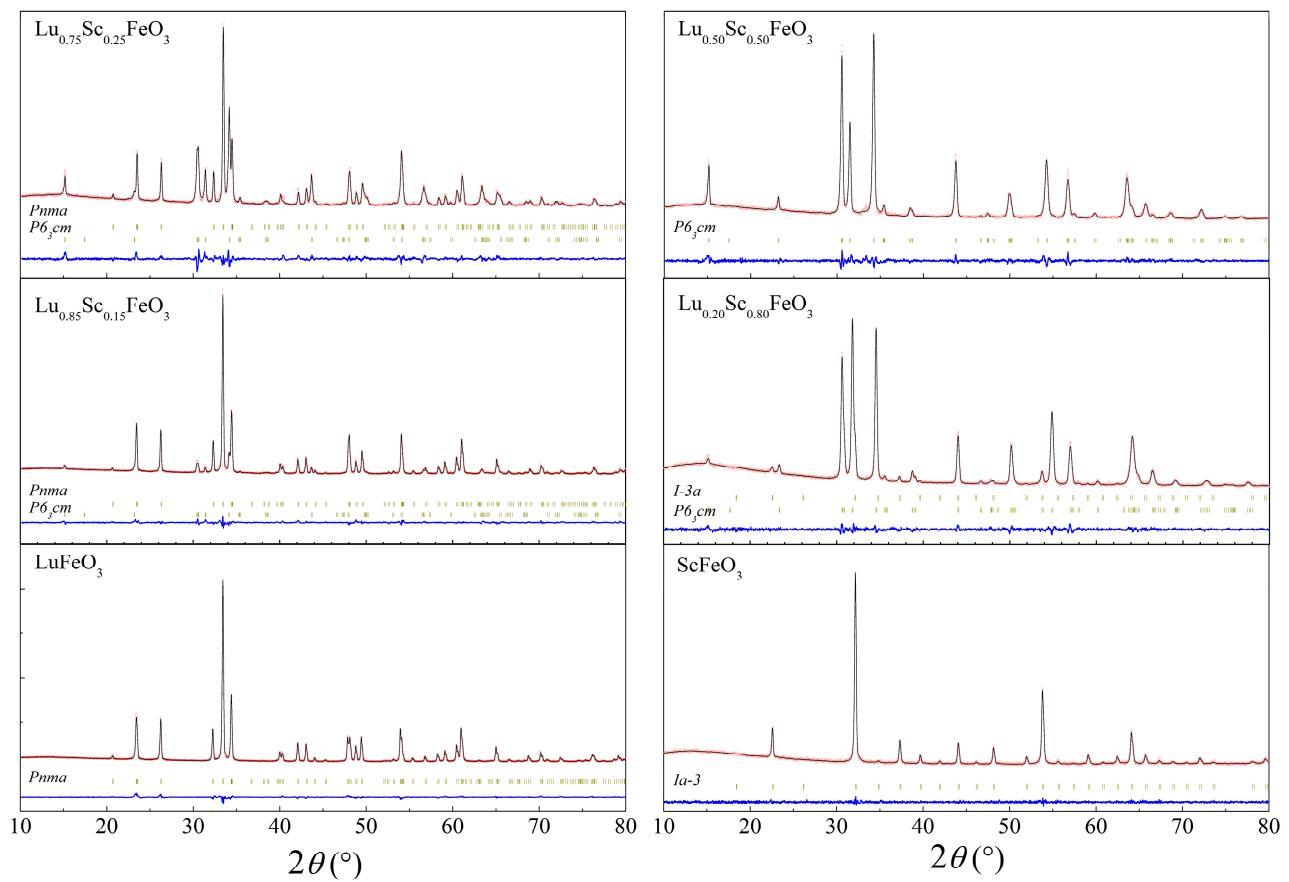
### 3. Results

#### 3.1. Crystal Structure of the Compounds by Diffraction Measurements

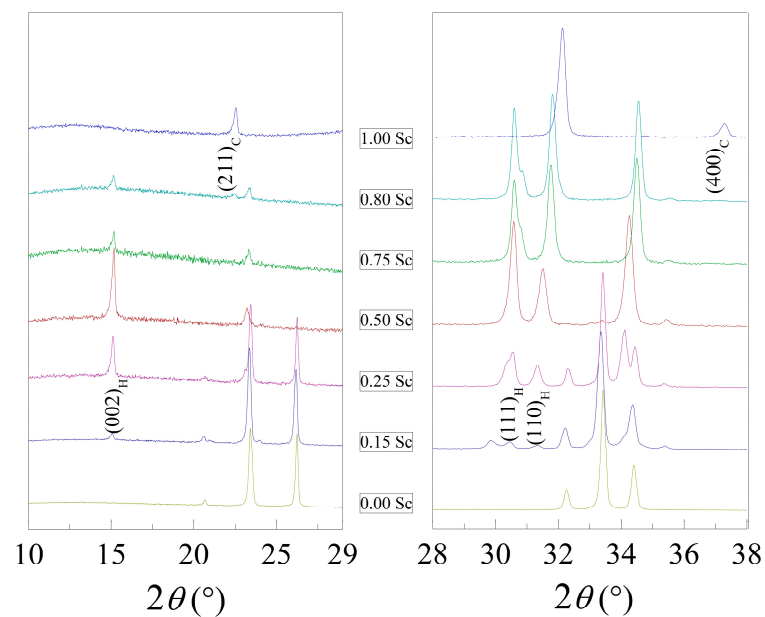
The diffraction data obtained for  $\text{LuFeO}_3$  (Figure S1) indicated the formation of an amorphous phase in the xerogels sintered at temperatures up to 650 °C. However, further increase in the temperature up to 800 °C led to the formation of a typical orthoferrite phase with orthorhombic symmetry, described by the  $Pnma$  (#62) space group [25]. An additional increase in temperature up to 950 and 1100 °C led to a narrowing of the diffraction peaks and a notable increase in their intensity, which was caused by increased crystallinity and crystallite size. A slightly different behavior was found for the  $\text{ScFeO}_3$  samples. Even at the initial sintering temperature of 650 °C, multiple diffraction peaks were observed, indicating the formation of a crystalline phase (Figure S2). This phase is consistent with the formation of a bixbyite-type structure of  $\text{ScFeO}_3$  having cubic symmetry and described by the space group  $Ia-3$  (#206); a small amount of an unidentified impurity phase was also observed. The mixed structural state was consistent up to 950 °C; however, the reflections specific for the bixbyite structure notably increased in intensity, relatively to the impurity phase. At the temperature of 1100 °C, a single-phase cubic bixbyite structure formed, but even in this case, the diffraction pattern was characterized by a quite high-intensity background, indicating a residual amorphous component and the need of an even higher sintering temperature. Furthermore, it is worthy to note that the bixbyite structure could no longer be considered a perovskite, since in the structure, the Sc and Fe ions were distributed randomly due to their relatively similar ionic radii.

The initial XRD patterns as well as the data refined by the Rietveld method are presented in Figures 1 and S3, which confirm the formation of the solid solutions over the whole concentration range and where several different structural phase regions are observed. As mentioned before, the compound  $\text{Lu}_{(1-x)}\text{Sc}_x\text{FeO}_3$  with  $x = 0$  is characterized by a single-phase orthorhombic structure (Figure 1); however, an even quite small doping level of 15 mole% already induced notable structural changes. These changes were expressed as the initial formation of an hexagonal phase described by the space group  $P6_3cm$  (#185), as indicated by the appearance of the reflections indexed as  $(110)_H$ ,  $(111)_H$  and located around  $2\theta \sim 30.44^\circ$  and the reflection  $(002)_H$  around  $2\theta \sim 14.45^\circ$  (Figure 2). This phase is usually considered quite unstable in the  $\text{LuFeO}_3$  matrix that is most often obtained in thin films because of a high strain occurring between the substrate and the film or in bulk compounds via chemical doping [15,34]. Upon further substitution of lutetium ions by scandium ions up to  $x = 0.50$ , a gradual increase in the volume fraction of the hexagonal phase was observed as the reflections specific to this phase increased in intensity. Meanwhile, the reflections attributed to the orthorhombic phase became less intensive and, in this case, disappeared completely, resulting in the stabilization of the single-phase hexagonal structure. The single-phase hexagonal structure was also observed for the compound having 75% of Sc content. A further increase of Sc up to 80% led to additional changes and to the appearance of a new phase. This new phase had a bixbyite structure, as shown by the appearance of new reflections indexed as  $(211)_C$  at around  $22.5^\circ$  and  $(400)_C$  at around  $37.2^\circ$  (Figure 2). When Lu ions were fully replaced by Sc ions, a single phase with the aforementioned structure was stabilized. Detailed structural data obtained by Rietveld analysis can be seen in Table 1. From these results, one can clearly see that the introduction of  $\text{Sc}^{3+}$  into the  $\text{LuFeO}_3$  matrix led to a decrease in the volume of orthorhombic lattice, while the unit cell parameters changed in different ways, e.g., the b-parameter firstly increased in the compounds with dopant content up to 15% but then started to decrease. Furthermore, the phase composition showed a gradual onset of the hexagonal phase, while at the initial 15% of scandium content, only a minor amount (9%) of the  $P6_3cm$  phase was present. Almost equal phase ratios were measured in the presence of around 25% of Sc dopant; for compounds with  $x = 50\%$  and  $75\%$ , the single-phase hexagonal structure was observed. When doping increased up to 80%, a cubic phase with a volume fraction of around 12% formed. The compound with 100% Sc content was single-phase with cubic structure. It is worthy to note that phase stability, as well as particle morphology and size, were notably affected by the synthesis conditions [26,27,35,36]. The structural data are summarized in the form of a phase diagram presented in Figure 3a.

Due to the aforementioned quite intensive background in the  $\text{ScFeO}_3$  sample, it was decided to further anneal the samples containing 0, 0.25, 0.50, 0.75, and 1 Sc at even higher temperatures of 1300 and 1500 °C. The diffraction patterns obtained for these samples can be seen in Figures S4–S8. No significant changes were observed for samples with 0, 0.50, and 1 Sc, besides the narrowing of the reflections, which was most likely caused by an increase of particle size. However, when considering the samples near the phase boundary, viz., those with  $x = 0.25, 0.75$ , the phase equilibrium seemed to be affected, as a higher synthesis temperature led to a phase transitions from  $Pnma$  to  $P6_3cm$  as well as from  $P6_3cm$  to  $Ia-3$  (Figure 3b–d). For the compound containing 25% of scandium ions, it was noticed that after calcination at 1300 °C, the volume fraction of the hexagonal phase increased from 46% to 60% and finally to 79% when the calcination temperature was 1500 °C. A similar case was observed for the compound with 75% of Sc ions, where the amount of the bixbyite phase increased from 0% at 1100 °C to 20% after calcination at 1300 °C and finally to 80% after sintering at 1500 °C. Overall, these phase transitions indicated that the phase composition and stability were highly affected by the synthesis conditions and could be adjusted accordingly.



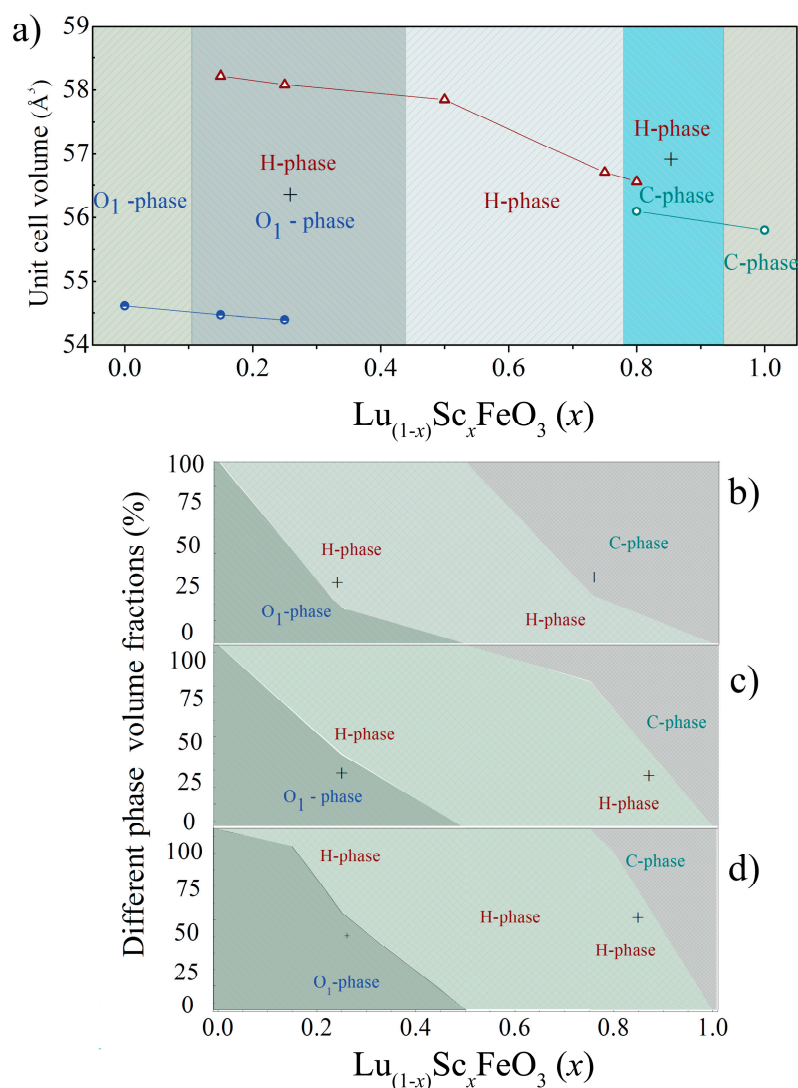
**Figure 1.** Rietveld refinement results of XRD data recorded for  $\text{Lu}_{(1-x)}\text{Sc}_x\text{FeO}_3$  ( $0 \leq x \leq 1.00$ ) compounds at room temperature (red dots are the experimental data; black lines are calculated data), Bragg reflections are indicated by vertical ticks.



**Figure 2.** Phase specific peaks for  $P6_3cm$  and  $Ia-3$  space groups.

**Table 1.** Unit cell parameters, reduced volume, and EDX results for  $\text{Lu}_{(1-x)}\text{Sc}_x\text{FeO}_3$  ( $0 \leq x \leq 1.00$ ) compounds calcinated at  $1100^\circ\text{C}$ .

Sample	Phase	$a$ , Å	$b$ , Å	$c$ , Å	Volume Å <sup>3</sup> (Per Reduced Cell)	Sc/(Sc + Lu) Ratio	(Sc + Lu)/Fe Ratio
$\text{LuFeO}_3$	$Pnma$	5.546(4)	7.557(5)	5.211(3)	54.60(6)	0.000	0.935
$\text{Lu}_{0.85}\text{Sc}_{0.15}\text{FeO}_3$	$Pnma$ (91%)	5.533(4)	7.564(2)	5.205(1)	54.46(2)	—	—
	$P6_3cm$ (9%)	5.875(8)	5.875(8)	11.688(7)	58.22(5)		
$\text{Lu}_{0.75}\text{Sc}_{0.25}\text{FeO}_3$	$Pnma$ (54%)	5.532(1)	7.560(5)	5.201(8)	54.39(2)	0.197	0.994
	$P6_3cm$ (46%)	5.869(9)	5.869(9)	11.682(2)	58.08(2)		
$\text{Lu}_{0.50}\text{Sc}_{0.50}\text{FeO}_3$	$P6_3cm$	5.856(1)	5.856(1)	11.690(1)	57.84(8)	0.447	0.932
$\text{Lu}_{0.25}\text{Sc}_{0.75}\text{FeO}_3$	$P6_3cm$	5.800(9)	5.800(9)	11.678(8)	56.70(7)	0.713	0.914
$\text{Lu}_{0.20}\text{Sc}_{0.80}\text{FeO}_3$	$P6_3cm$ (88%)	5.793(9)	5.793(9)	11.676(1)	56.55(8)	—	—
	$Ia-3$ (12%)	9.646(1)	9.646(1)	9.646(1)	56.09(5)		
$\text{ScFeO}_3$	$Ia-3$	9.629(4)	9.629(4)	9.629(4)	55.80(6)	1.00	1.002

**Figure 3.** Concentration-driven phase diagram (a). Volume fractions of different phases for compounds prepared at high temperatures of  $1500^\circ\text{C}$ —(b),  $1300^\circ\text{C}$ —(c),  $1100^\circ\text{C}$ —(d).

### 3.2. Raman Spectroscopy Analysis

Raman spectroscopy was employed to access the short-range structural details of the studied compounds. In addition, this technique sensitively probes the presence of defects and disorders [37–39]. Figure 4a compares 532 nm excited Raman spectra of polycrystalline LuFeO<sub>3</sub> and ScFeO<sub>3</sub> samples sintered at 1100 °C. In the case of orthorhombic orthoferrites with a Pnma space group, one can expect 24 first-order Raman active modes distributed by symmetry in the following way [40,41]:

$$\Gamma_{Raman} = 7A_g + 5B_{1g} + 7B_{2g} + 5B_{3g} \quad (1)$$

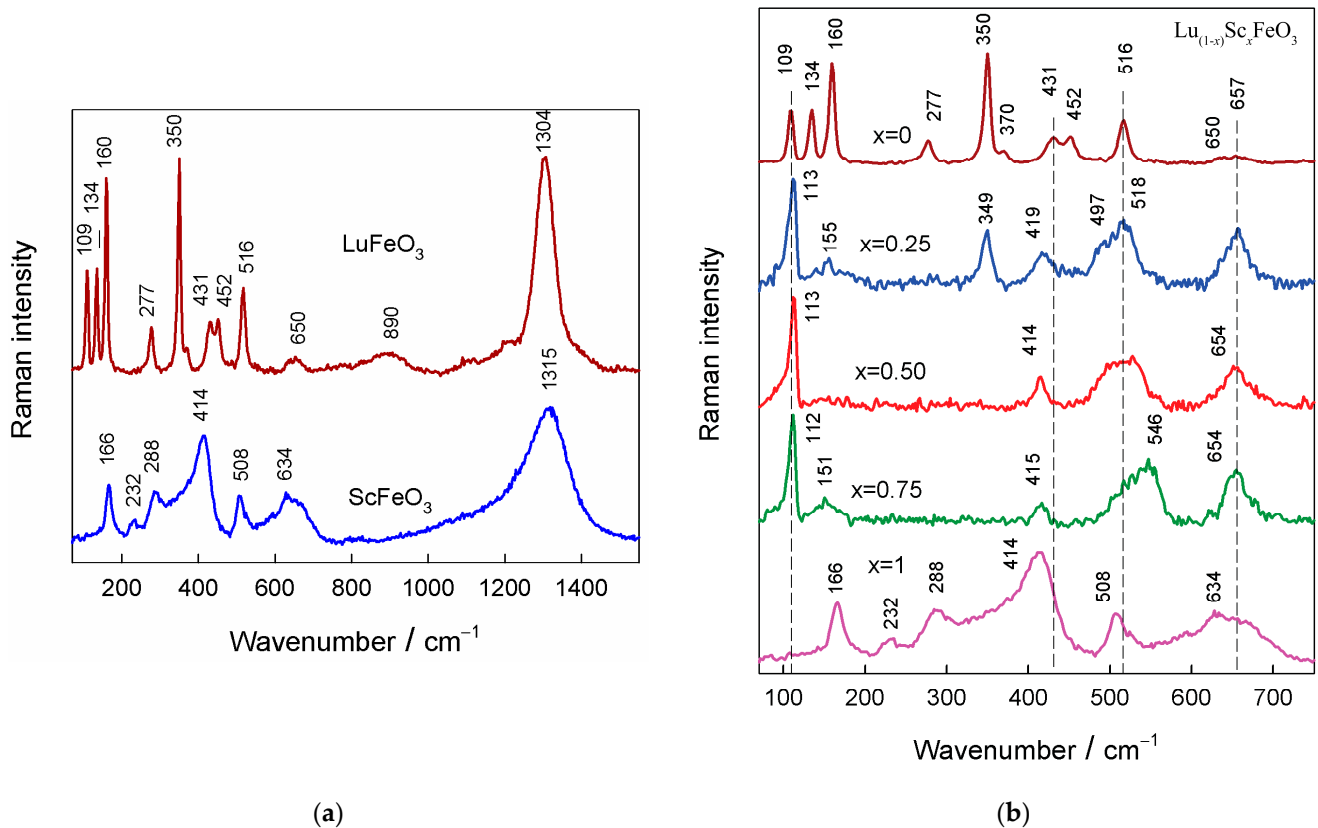


**Figure 4.** Raman spectra of polycrystalline LuFeO<sub>3</sub> and ScFeO<sub>3</sub> (a). Composition-dependent Raman spectra of polycrystalline Lu<sub>(1-x)</sub>Sc<sub>x</sub>FeO<sub>3</sub> compounds. Intensities are normalized to the intensity of the most intense band, and the spectra are shifted vertically for clarity (b).

The positions of the fundamental bands were very similar to those in the Raman spectrum of a single-crystal LuFeO<sub>3</sub> sample [40], thus indicating a high phase purity of the studied compound. Based on the frequency value, the vibrational bands below ~200 cm<sup>-1</sup> could be considered associated mainly with vibrations of heavy rare-earth ions, the vibrational modes ranging from 200 to 350 cm<sup>-1</sup> could be related to tilting motions of FeO<sub>6</sub> octahedra, the bands in the frequency region from 350 to 500 cm<sup>-1</sup> belonged mainly to the oxygen bending modes, and the vibrational modes at wavenumbers higher than 500 cm<sup>-1</sup> were related to symmetric stretching vibrations of Fe–O bonds [41,42].

The compound ScFeO<sub>3</sub> exhibited a completely different spectral pattern (Figure 4a). To the best of our knowledge, there no Raman spectrum of this compound is available in the literature. The XRD measurements indicated the formation of a bixbyite structure having cubic symmetry, described by the space group *Ia-3*. The most intense Raman band for such structure was expected for the *F<sub>g</sub>* symmetry vibrational mode [43,44]. The corresponding band in the spectrum of the compound was visible near 414 cm<sup>-1</sup> (*F<sub>g</sub>*). The other same symmetry modes were observed at 288 cm<sup>-1</sup> (*F<sub>g</sub>*) and 508 cm<sup>-1</sup> (*F<sub>g</sub>*). The

clearly resolved low-frequency band at  $166\text{ cm}^{-1}$  probably belonged to the  $E_g$  symmetry vibrational mode [43]. The broad band near  $634\text{ cm}^{-1}$  had a high contribution from the two-phonon vibrational mode.

Figure 4b shows the composition-induced changes in the Raman spectra of  $\text{Lu}_{(1-x)}\text{Sc}_x\text{FeO}_3$  compounds in the frequency region of  $70\text{--}750\text{ cm}^{-1}$ . As discussed above, the spectrum of compound  $\text{LuFeO}_3$  was characteristic of the orthorhombic phase. However, the spectrum of compound with  $x = 0.25$  demonstrated prominent structural changes. The intensity of the bands characteristic of the orthorhombic phase near  $134$  and  $160\text{ cm}^{-1}$  considerably decreased, while other lower relative intensity characteristic modes near  $277$  and  $452\text{ cm}^{-1}$  completely disappeared. However, the intensity of the prominent band near  $350\text{ cm}^{-1}$  decreased in about times. Importantly, the width of the band determined as full width at half maximum (FWHM) increased from  $8.6$  to  $14.1\text{ cm}^{-1}$ . This indicated a considerable distortion of the local structure of the remaining orthorhombic phase. In addition, new intense bands were visible at  $113$ ,  $419$ ,  $497$ , and  $657\text{ cm}^{-1}$ . The newly appeared bands were characteristic of the hexagonal phase of  $\text{LuFeO}_3$  and similar compounds [27,45–49]. For the non-centrosymmetric hexagonal crystal symmetry with the  $P6_3\text{cm}$  space group, one can expect to observe 38 Raman-active modes distributed by symmetry in the following manner [46,47,49]:

$$\Gamma_{\text{Raman}} = 9A_1 + 14E_1 + 15E_2 \quad (2)$$

The most intense band located at  $113\text{ cm}^{-1}$  belonged to the  $E_2$  symmetry vibrational mode and can be described as the vibration mode of the heavy Lu ion [47]. The relatively broad band near  $419\text{ cm}^{-1}$  ( $E_1$ ) was attributed to Lu–O stretching vibration, while the shoulder near  $497\text{ cm}^{-1}$  ( $A_1$ ) had a high contribution from the  $\text{FeO}_6$  group bending vibration [47]. Finally, the strong and broad feature at  $657\text{ cm}^{-1}$  ( $A_1$ ) was mainly related to Fe–O stretching motion. Thus, the Raman data indicated the coexistence of the two phases (orthorhombic and hexagonal) for the compound with  $x = 0.25$ . In addition, the local structure of the orthorhombic phase was highly disordered. The increase in the amount of Sc ions up to  $x = 0.50$  resulted in the complete disappearance of the bands characteristic of the orthorhombic phase. This might be related to the transformation of the orthorhombic phase to the hexagonal phase or to the presence of a small amount of highly disordered local structure of the orthorhombic phase. The FWHM value of the band of to the hexagonal phase at  $414\text{ cm}^{-1}$  decreased from  $24.0\text{ cm}^{-1}$ , in the case of the sample with  $x = 0.25$ , to  $15.4\text{ cm}^{-1}$  for the compound with  $x = 0.50$ , indicating a local structure ordering in the hexagonal phase. Further increase in the amount of Sc ions ( $x = 0.75$ ) resulted only in a perturbation of the complex Raman band near  $520\text{ cm}^{-1}$ . This band had two components located near  $523$  and  $546\text{ cm}^{-1}$ ; the higher-frequency blue-shifted component clearly appeared for the compound with  $x = 0.75$ . Because the vibrational modes in the frequency region above  $500\text{ cm}^{-1}$  are related mainly to Fe–O stretching vibrations [41,42], this may indicate a strengthening of the corresponding bond. It should be noted that the spectral parameters of the strong band near  $112\text{ cm}^{-1}$  remained essentially unchanged, which suggested that the local structure in the vicinity of heavy Lu ions remained similar.

### 3.3. Scanning Electron Microscopy and EDX Analysis

SEM measurements allowed investigating the effect of Sc doping on crystallite morphology and phase stability (Figure 5). The particle size was measured using ImageJ software and is presented in Figure 6 [50]. The initial compound ( $x = 0$ ) with a single-phase orthorhombic structure was characterized by a rectangular-like shape of the particles, which corresponds to the symmetry of a crystal lattice [51]. The particle size in this compound varied from  $\sim 0.05$  to  $0.45\text{ }\mu\text{m}$ , with an average value of  $\sim 0.19\text{ }\mu\text{m}$ . Increasing the scandium content up to 25%, led to significant changes in particle morphology and revealed two distinct regions. One region (region #1) was associated with crystallites of rectangular shape with extremely sharp and discrete edges, while the other region (region #2) was characterized by crystallites with diffuse edges and smeared borders between the individual particles. Furthermore, the average particle size decreased to  $\sim 0.16\text{ }\mu\text{m}$ . In the compound



with 50% Sc content, the number of particles with diffuse edges was much greater, while the average particle size further decreased to  $\sim 0.14 \mu\text{m}$ . In the compound having 75% Sc content, this trend reached its maximum. SEM data confirmed the model which assumes the formation of particle clusters with no clear borders between each particle, so that the individual particles can scarcely be observed. As such, the average particle size is difficult to determine correctly, and we estimated it to be around  $\sim 0.09 \mu\text{m}$ . The compound without lutetium was characterized by a drastically different morphology of the crystallites, compared to the compounds having a mixed structural state or the hexagonal phase, which mostly resembled the morphology specific for the initial compound  $\text{LuFeO}_3$ . The particles had a semi-spherical shape and a particle size in the range from 0.05 to  $0.3 \mu\text{m}$ , with an average size of about  $0.12 \mu\text{m}$ . A broad particle size distribution is quite common for compounds prepared by the sol–gel technique [52–54]. Overall, the changes in particle morphology could be related to the change in crystal structure, as the compound with mixed structural state (e.g.,  $x = 0.25$ ) or single-phase hexagonal structure (e.g.,  $x = 0.50, 0.75$ ) were characterized by a different morphology of the particles. The highest number of particles with no distinct shape and clear borders was most found in compounds with a dominant hexagonal structure. Furthermore, the average particle size decreased with the increase of scandium content, which indicated hampering of the grain growth. This was most likely related to the changes of the melting point of the final compound, as such effects have been previously reported to cause similar changes in particle size [55].

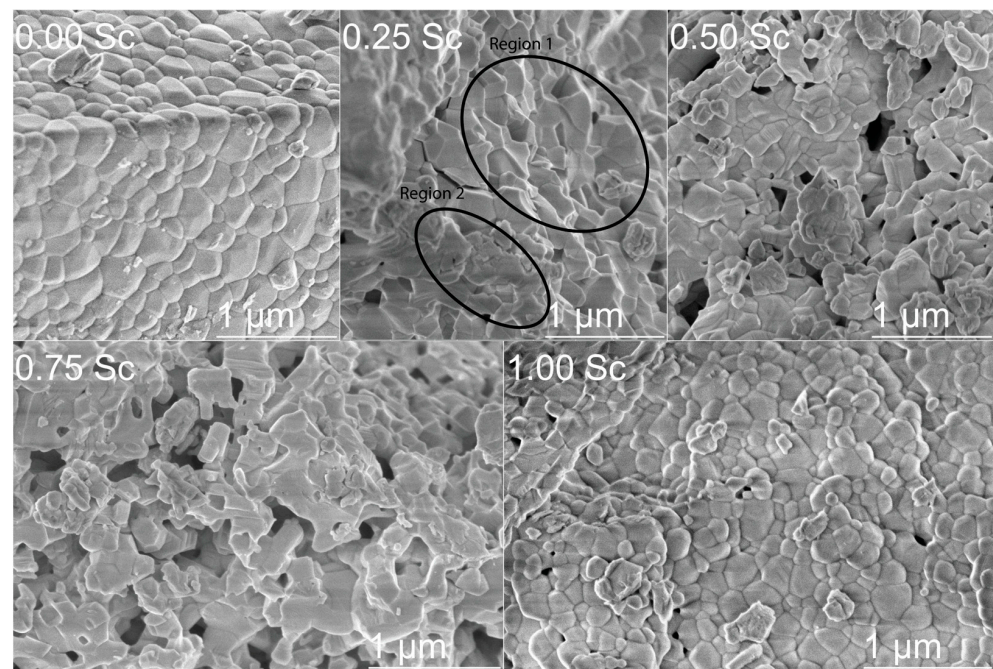


**Figure 5.** SEM micrographs of  $\text{Lu}_{(1-x)}\text{Sc}_x\text{FeO}_3$  ( $x = 0, 0.25, 0.50, 0.75, 1.00$ ) samples.

In  $\text{LuFeO}_3$ -based compounds, even slight deviations from the intended chemical composition can cause changes in phase transitions and phase stability [56,57]. As such, it is important to further investigate the chemical composition of the samples, and for this reason, EDS measurements were performed. For the initial compound without Sc, the Lu/Fe ratio was measured to be 0.935 (theoretical value was 1), which indicated a homogeneous distribution of the related ions in the sample. In the compound with 25% Sc content, it was observed that the ratio of  $(\text{Sc} + \text{Lu})/\text{Fe}$  was 0.994, also quite close to the theoretical value. Similar results were observed for the other samples as well for that with  $x = 0.50$ , where the ratio of  $(\text{Sc} + \text{Lu})/\text{Fe}$  was 0.932, for that with 75% Sc content that had a ratio of 0.914, and for that with 100% Sc, with a ratio of 1.002 (Table 1). While all samples showed a quite homogeneous distribution, the largest difference between the theoretical

values was observed for the compounds near the phase boundaries, especially for the compound with 75% Sc content.

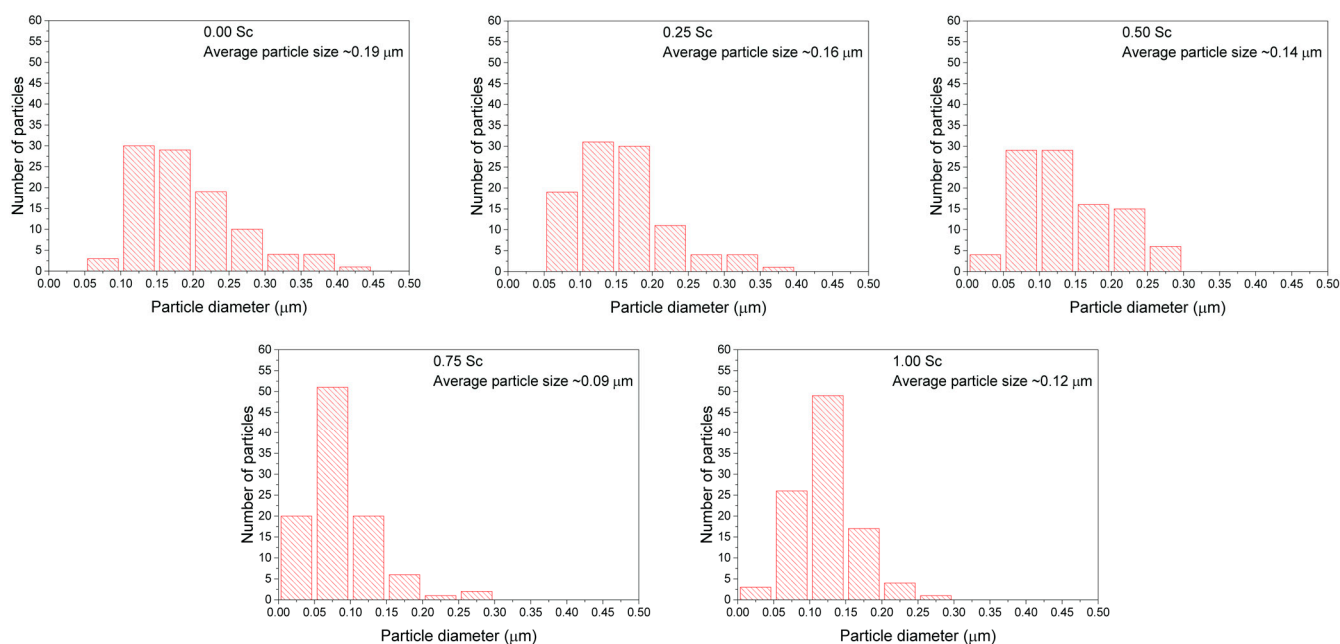


**Figure 6.** Particle size histograms of  $\text{Lu}_{(1-x)}\text{Sc}_x\text{FeO}_3$  ( $x = 0, 0.25, 0.50, 0.75, 1.00$ ) samples.

Furthermore, from the EDS data, it was determined that the ratio of  $\text{Sc}/(\text{Lu} + \text{Sc})$  was also quite close to the theoretical value for all samples, with a difference of around 3–6%; only for compound having 0.75 of Sc, a higher difference was observed, this potentially caused by inaccuracies during the measurements. Overall, a quite homogeneous distribution of all elements was observed, with no drastic loss or increase in any element. This showed the occurrence of atomic-level mixing of the precursors during the preparation of the compounds using the sol–gel method.

#### 4. Conclusions

A sol–gel method was used to synthesize the compounds  $\text{Lu}_{(1-x)}\text{Sc}_x\text{FeO}_3$  ( $0 \leq x \leq 1$ ) with high phase purity. The compounds with  $x < 0.15$  were characterized by a single-phase structural state with orthorhombic structure described by the space group  $Pnma$ ; increase in the concentration of Sc ions led to a structural transition to the hexagonal phase (sp. gr.  $P6_3cm$ ) via a two-phase structural state for the concentration range  $0.15 < x < 0.45$ ; further chemical doping caused the formation of the single-phase non-perovskite bixbyite structure (sp. gr.  $Ia-3$ ) via two-phase regions, as confirmed by the X-ray diffraction and Raman spectroscopy data. The concentration ranges of the mixed structural states were notably dependent on the synthesis conditions; thus, a high-temperature annealing of the compounds within the morphotropic phase boundary stabilized the phase-specific structure for the heavily doped compounds, viz., the hexagonal phase for the compounds with  $0.1 < x < 0.4$  and the bixbyite structure for the compounds with  $x \geq 0.8$ . A strong correlation between the type of structural distortion and the morphology of the crystallites was observed and analyzed, focusing on the compounds with a mixed structural state. Chemical doping also caused a reduction of the average crystalline size from  $\sim 0.2 \mu\text{m}$  for the undoped compounds, down to  $\sim 0.1 \mu\text{m}$  for the heavily doped compounds. Based on the structural data, a preliminary composition-dependent phase diagram was constructed, showing the concentration ranges of the single-phase and the mixed-structural-phase regions.

**Supplementary Materials:** The following supporting information can be downloaded at: <https://www.mdpi.com/article/10.3390/ma15031048/s1>, Figure S1: XRD patterns of LuFeO<sub>3</sub> prepared at different sintering temperatures, Figure S2: XRD patterns of ScFeO<sub>3</sub> prepared at different sintering temperatures, Figure S3: XRD patterns of Lu<sub>(1-x)</sub>Sc<sub>x</sub>FeO<sub>3</sub> (0 ≤ x ≤ 1), Figure S4: XRD patterns of LuFeO<sub>3</sub> additionally calcinated at different temperatures, Figure S5: XRD patterns of Lu<sub>0.75</sub>Sc<sub>0.25</sub>FeO<sub>3</sub> additionally calcinated at different temperatures, Figure S6: XRD patterns of Lu<sub>0.50</sub>Sc<sub>0.50</sub>FeO<sub>3</sub> additionally calcinated at different temperatures, Figure S7: XRD patterns of Lu<sub>0.25</sub>Sc<sub>0.75</sub>FeO<sub>3</sub> additionally calcinated at different temperatures, Figure S8: XRD patterns of ScFeO<sub>3</sub> additionally calcinated at different temperatures.

**Author Contributions:** Data curation, A.Z.; Formal analysis, D.O.A., A.P.T., A.L.Z., M.V.S., D.V.Z. and G.N.; Funding acquisition, D.V.K. and A.K.; Investigation, A.P., D.O.A., A.P.T., A.L.Z., M.V.S., D.V.Z. and G.N.; Methodology, A.P. and R.S.; Resources, A.K.; Supervision, R.S. and D.V.K.; Visualization, A.Z.; Writing—original draft, A.P.; Writing—review & editing, D.V.K. and A.K. All authors have read and agreed to the published version of the manuscript.

**Funding:** This project received funding from the European Union’s Horizon 2020 research and innovation programme under the Marie Skłodowska-Curie grant agreement No 778070—TransFERR—H2020-MSCA-RISE-2017. G.N. gratefully acknowledges the Center of Spectroscopic Characterization of Materials and Electronic/Molecular Processes (SPECTROVERSUM Infrastructure) for use of Raman spectrometer. A.L.Z. and A.P.T. acknowledge BRFFR (project # T21RM-040) and RFBR (project # 20-52-04011) respectively. M.V.S. acknowledges Ministry of Science and Higher Education of the Russian Federation within the framework of state support for the creation and development of World-Class Research Centers “Digital biodesign and personalized healthcare” #0075-15-2020-926. D.A. acknowledges the project CICECO- Aveiro Institute of Materials, UIDB/50011/2020 & UIDP/50011/2020, financed by national funds through the FCT/MEC and when appropriate co-financed by FEDER under the PT2020 Partnership Agreement.

**Data Availability Statement:** Not applicable.

**Conflicts of Interest:** The authors declare no conflict of interest. The funders had no role in the design of the study; in the collection, analyses, or interpretation of data; in the writing of the manuscript, or in the decision to publish the results.

## References

1. Ishihara, T. Inorganic perovskite oxides. In *Springer Handbooks*; Springer: Berlin/Heidelberg, Germany, 2017; p. 1.
2. Song, Z.; Zhao, J.; Liu, Q. Luminescent perovskites: Recent advances in theory and experiments. *Inorg. Chem. Front.* **2019**, *6*, 2969–3011. [[CrossRef](#)]
3. Liu, H.; Yang, X. A brief review on perovskite multiferroics. *Ferroelectrics* **2017**, *507*, 69–85. [[CrossRef](#)]
4. Lone, I.H.; Aslam, J.; Radwan, N.R.E.; Bashal, A.H.; Ajlouni, A.F.A.; Akhter, A. Multiferroic ABO<sub>3</sub> Transition Metal Oxides: A Rare Interaction of Ferroelectricity and Magnetism. *Nanoscale Res. Lett.* **2019**, *14*, 1–12. [[CrossRef](#)]
5. Shojaei, F.; Yin, W.J. Stability Trend of Tilted Perovskites. *J. Phys. Chem. C* **2018**, *122*, 15214–15219. [[CrossRef](#)]
6. Sato, T.; Takagi, S.; Deledda, S.; Hauback, B.C.; Orimo, S.I. Extending the applicability of the Goldschmidt tolerance factor to arbitrary ionic compounds. *Sci. Rep.* **2016**, *6*, 23592. [[CrossRef](#)]
7. Bartel, C.J.; Sutton, C.; Goldsmith, B.R.; Ouyang, R.; Musgrave, C.B.; Ghiringhelli, L.M.; Scheffler, M. New tolerance factor to predict the stability of perovskite oxides and halides. *Sci. Adv.* **2019**, *5*, eaav0693. [[CrossRef](#)]
8. Kumar, M.; Kumar, A.; Anshul, A.; Sharma, S. Advances and future challenges in multifunctional nanostructures for their role in fast, energy efficient memory devices. *Mater. Lett.* **2020**, *277*, 128369. [[CrossRef](#)]
9. Hill, N.A. Why are there so few magnetic ferroelectrics? *J. Phys. Chem. B* **2000**, *104*, 6694–6709. [[CrossRef](#)]
10. Fiebig, M.; Lottermoser, T.; Meier, D.; Trassin, M. The evolution of multiferroics. *Nat. Rev. Mater.* **2016**, *1*, 16046. [[CrossRef](#)]
11. Spaldin, N.A.; Ramesh, R. Advances in magnetoelectric multiferroics. *Nat. Mater.* **2019**, *18*, 203–212. [[CrossRef](#)]
12. Kalinkin, A.N.; Kozhbakhteev, E.M.; Polyakov, A.E.; Skorikov, V.M. Application of BiFeO<sub>3</sub> and Bi<sub>4</sub>Ti<sub>3</sub>O<sub>12</sub> in ferroelectric memory, phase shifters of a phased array, and microwave HEMTs. *Inorg. Mater.* **2013**, *49*, 1031–1043. [[CrossRef](#)]
13. Lu, C.; Wu, M.; Lin, L.; Liu, J.M. Single-phase multiferroics: New materials, phenomena, and physics. *Natl. Sci. Rev.* **2019**, *6*, 653–668. [[CrossRef](#)]
14. Čebela, M.; Zagorac, D.; Batalović, K.; Radaković, J.; Stojadinović, B.; Spasojević, V.; Hercigonja, R. BiFeO<sub>3</sub> perovskites: A multidisciplinary approach to multiferroics. *Ceram. Int.* **2017**, *43*, 1256–1264. [[CrossRef](#)]
15. Lin, L.; Zhang, H.M.; Liu, M.F.; Shen, S.; Zhou, S.; Li, D.; Wang, X.; Yan, Z.B.; Zhang, Z.D.; Zhao, J.; et al. Hexagonal phase stabilization and magnetic orders of multiferroic Lu<sub>1-x</sub>Sc<sub>x</sub>FeO<sub>3</sub>. *Phys. Rev. B* **2016**, *93*, 075146. [[CrossRef](#)]

16. Moyer, J.A.; Misra, R.; Mundy, J.A.; Brooks, C.M.; Heron, J.T.; Muller, D.A.; Schlom, D.G.; Schiffer, P. Intrinsic magnetic properties of hexagonal LuFeO<sub>3</sub> and the effects of nonstoichiometry. *APL Mater.* **2014**, *2*, 012106. [[CrossRef](#)]
17. Jeong, Y.K.; Lee, J.-H.; Ahn, S.-J.; Jang, H.M. Epitaxially Constrained Hexagonal Ferroelectricity and Canted Triangular Spin Order in LuFeO<sub>3</sub> Thin Films. *Chem. Mater.* **2012**, *24*, 2426–2428. [[CrossRef](#)]
18. Wang, W.; Zhao, J.; Wang, W.; Gai, Z.; Balke, N.; Chi, M.; Lee, H.N.; Tian, W.; Zhu, L.; Cheng, X.; et al. Room-temperature multiferroic hexagonal LuFeO<sub>3</sub> films. *Phys. Rev. Lett.* **2013**, *110*, 237601. [[CrossRef](#)]
19. Akbashev, A.R.; Semisalova, A.S.; Perov, N.S.; Kaul, A.R. Weak ferromagnetism in hexagonal orthoferrites RFeO<sub>3</sub> (R = Lu, Er-Tb). *Appl. Phys. Lett.* **2011**, *99*, 122502. [[CrossRef](#)]
20. Cao, S.; Zhang, X.; Paudel, T.R.; Sinha, K.; Wang, X.; Jiang, X.; Wang, W.; Brutsche, S.; Wang, J.; Ryan, P.J.; et al. On the structural origin of the single-ion magnetic anisotropy in LuFeO<sub>3</sub>. *J. Phys. Condens. Matter* **2016**, *28*, 156001. [[CrossRef](#)]
21. Gibbs, A.S.; Knight, K.S.; Lightfoot, P. High-temperature phase transitions of hexagonal YMnO<sub>3</sub>. *Phys. Rev. B Condens. Matter Mater. Phys.* **2011**, *83*, 094111. [[CrossRef](#)]
22. Luxová, J.; Šulcová, P. The effect of partial substitution of Bi on colour properties and thermal stability of Bi<sub>x</sub>Pr<sub>1-x</sub>FeO<sub>3</sub> pigments. *J. Therm. Anal. Calorim.* **2019**, *138*, 4303–4312. [[CrossRef](#)]
23. Wang, W.; Sun, W.; Zhang, G.; Cheng, Z.; Wang, Y. Magnetic domain-wall induced ferroelectric polarization in rare-earth orthoferrites AFeO<sub>3</sub> (A = Lu, Y, Gd): First-principles calculations. *J. Mater. Chem. C* **2019**, *7*, 10059–10065. [[CrossRef](#)]
24. Wang, Z.Q.; Lan, Y.S.; Zeng, Z.Y.; Chen, X.R.; Chen, Q.F. Magnetic structures and optical properties of rare-earth orthoferrites RFeO<sub>3</sub> (R = Ho, Er, Tm and Lu). *Solid State Commun.* **2019**, *288*, 10–17. [[CrossRef](#)]
25. Zhang, L.; Chen, X.M. Dielectric relaxation in LuFeO<sub>3</sub> ceramics. *Solid State Commun.* **2009**, *149*, 1317–1321. [[CrossRef](#)]
26. Deng, S.; Li, J.; Småbråten, D.R.; Shen, S.; Wang, W.; Zhao, J.; Tao, J.; Aschauer, U.; Chen, J.; Zhu, Y.; et al. Critical Role of Sc Substitution in Modulating Ferroelectricity in Multiferroic LuFeO<sub>3</sub>. *Nano Lett.* **2021**, *21*, 6648–6655. [[CrossRef](#)]
27. White, J.; Sinha, K.; Xu, X. Structural phase diagram and magnetic properties of Sc-substituted rare earth ferrites R<sub>1-x</sub>Sc<sub>x</sub>FeO<sub>3</sub> (R = Lu, Yb, Er, and Ho). *J. Appl. Phys.* **2019**, *125*, 244101. [[CrossRef](#)]
28. Suresh, P.; Vijaya Laxmi, K.; Anil Kumar, P.S. Enhanced room temperature multiferroic characteristics in hexagonal LuFe<sub>1-x</sub>Ni<sub>x</sub>O<sub>3</sub> (x = 0 – 0.3) nanoparticles. *J. Magn. Magn. Mater.* **2018**, *448*, 117–122. [[CrossRef](#)]
29. Disseler, S.M.; Luo, X.; Gao, B.; Oh, Y.S.; Hu, R.; Wang, Y.; Quintana, D.; Zhang, A.; Huang, Q.; Lau, J.; et al. Multiferroicity in doped hexagonal LuFeO<sub>3</sub>. *Phys. Rev. B* **2015**, *92*, 54435. [[CrossRef](#)]
30. Pęczkowski, P.; Zachariasz, P.; Kowalik, M.; Zalecki, R.; Jastrzębski, C. Characterization of the superconductor-multiferroic type materials based on YBa<sub>2</sub>Cu<sub>3</sub>O<sub>7-δ</sub>-YMnO<sub>3</sub> composites. *Ceram. Int.* **2019**, *45*, 18189–18204. [[CrossRef](#)]
31. Pęczkowski, P.; Zachariasz, P.; Kowalik, M.; Tokarz, W.; Kumar Naik, S.P.; Żukrowski, J.; Jastrzębski, C.; Dadiel, L.J.; Tabiś, W.; Gondek, Ł. Iron diffusivity into superconducting YBa<sub>2</sub>Cu<sub>3</sub>O<sub>7-δ</sub> at oxygen-assisted sintering: Structural, magnetic, and transport properties. *J. Eur. Ceram. Soc.* **2021**, *41*, 7085–7097. [[CrossRef](#)]
32. Du, K.; Gao, B.; Wang, Y.; Xu, X.; Kim, J.; Hu, R.; Huang, F.T.; Cheong, S.W. Vortex ferroelectric domains, large-loop weak ferromagnetic domains, and their decoupling in hexagonal (Lu, Sc)FeO<sub>3</sub>. *Npj Quantum Mater.* **2018**, *3*, 33. [[CrossRef](#)]
33. Rodríguez-Carvajal, J. Recent advances in magnetic structure determination by neutron powder diffraction. *Phys. B Condens. Matter* **1993**, *192*, 55–69. [[CrossRef](#)]
34. Xu, X.; Wang, W. Multiferroic hexagonal ferrites (h-RFeO<sub>3</sub>, R = Y, Dy-Lu): A brief experimental review. *Mod. Phys. Lett. B* **2014**, *28*, 1430008. [[CrossRef](#)]
35. Jo, W.; Kim, T.H.; Kim, D.Y.; Pabi, S.K. Effects of grain size on the dielectric properties of Pb (Mg<sub>1/3</sub>Nb<sub>2/3</sub>) O<sub>3</sub>-30 mol % PbTiO<sub>3</sub> ceramics. *J. Appl. Phys.* **2007**, *102*, 074116. [[CrossRef](#)]
36. Behera, C.; Choudhary, R.N.P.; Das, P.R. Structural, electrical and multiferroic characteristics of thermo-mechanically fabricated BiFeO<sub>3</sub>-(BaSr)TiO<sub>3</sub> solid solutions. *Mater. Res. Express* **2018**, *5*, 056301. [[CrossRef](#)]
37. Pakalniškis, A.; Lukowiak, A.; Niaura, G.; Głuchowski, P.; Karpinsky, D.V.; Alikin, D.O.; Abramov, A.S.; Zhaludkevich, A.; Silibin, M.; Kholkin, A.L.; et al. Nanoscale ferroelectricity in pseudo-cubic sol-gel derived barium titanate—Bismuth ferrite (BaTiO<sub>3</sub>-BiFeO<sub>3</sub>) solid solutions. *J. Alloy. Compd.* **2020**, *830*, 154632. [[CrossRef](#)]
38. Karoblis, D.; Zarkov, A.; Mazeika, K.; Baltrunas, D.; Niaura, G.; Beganskiene, A.; Kareiva, A. Sol-gel synthesis, structural, morphological and magnetic properties of BaTiO<sub>3</sub>-BiMnO<sub>3</sub> solid solutions. *Ceram. Int.* **2020**, *46*, 16459–16464. [[CrossRef](#)]
39. Trusovas, R.; Račiukaitis, G.; Niaura, G.; Barkauskas, J.; Valušis, G.; Pauliukaite, R. Recent Advances in Laser Utilization in the Chemical Modification of Graphene Oxide and Its Applications. *Adv. Opt. Mater.* **2016**, *4*, 37–65. [[CrossRef](#)]
40. Venugopalan, S.; Becker, M.M. Raman scattering study of LuFeO<sub>3</sub>. *J. Chem. Phys.* **1998**, *93*, 3833. [[CrossRef](#)]
41. Wang, Z.; Xiao, W.; Zhang, J.; Huang, J.; Dong, M.; Yuan, H.; Xu, T.; Shi, L.; Dai, Y.; Liu, Q.; et al. Effects of mechanochemical activation on the structural and electrical properties of orthorhombic LuFeO<sub>3</sub> ceramics. *J. Am. Ceram. Soc.* **2021**, *104*, 3019–3029. [[CrossRef](#)]
42. Ahmad Mir, F.; Ikram, M.; Kumar, R. Temperature-dependent Raman study of PrFeO<sub>3</sub> thin film. *J. Raman Spectrosc.* **2011**, *42*, 201–208. [[CrossRef](#)]
43. Ibáñez, J.; Blázquez, O.; Hernández, S.; Garrido, B.; Rodríguez-Hernández, P.; Muñoz, A.; Velázquez, M.; Veber, P.; Manjón, F.J. Lattice dynamics study of cubic Tb<sub>2</sub>O<sub>3</sub>. *J. Raman Spectrosc.* **2018**, *49*, 2021–2027. [[CrossRef](#)]
44. Abrashev, M.V.; Todorov, N.D.; Geshev, J. Raman spectra of R<sub>2</sub>O<sub>3</sub> (R—Rare earth) sesquioxides with C-type bixbyite crystal structure: A comparative study. *J. Appl. Phys.* **2014**, *116*, 103508. [[CrossRef](#)]

45. Disseler, S.M.; Borchers, J.A.; Brooks, C.M.; Mundy, J.A.; Moyer, J.A.; Hillsberry, D.A.; Thies, E.L.; Tenne, D.A.; Heron, J.; Holtz, M.E.; et al. Magnetic structure and ordering of multiferroic hexagonal LuFeO<sub>3</sub>. *Phys. Rev. Lett.* **2015**, *114*, 217602. [[CrossRef](#)]
46. Suresh, P.; Vijaya Laxmi, K.; Bera, A.K.; Yusuf, S.M.; Chittari, B.L.; Jung, J.; Anil Kumar, P.S. Magnetic ground state of the multiferroic hexagonal LuFeO<sub>3</sub>. *Phys. Rev. B* **2018**, *97*, 184419. [[CrossRef](#)]
47. Chaturvedi, S.; Shyam, P.; Shirolkar, M.M.; Krishna, S.S.; Sinha, B.; Caliebe, W.; Kalinko, A.; Srinivasan, G.; Ogale, S. Unusual magnetic ordering transitions in nanoscale biphasic LuFeO<sub>3</sub>: The role of the ortho-hexa phase ratio and the local structure. *J. Mater. Chem. C* **2020**, *8*, 17000–17008. [[CrossRef](#)]
48. Smith, K.A.; Ramkumar, S.P.; Harms, N.C.; Clune, A.J.; Cheong, S.W.; Liu, Z.; Nowadnick, E.A.; Musfeldt, J.L. Pressure-induced phase transition and phonon softening in h-Lu<sub>0.6</sub>Sc<sub>0.4</sub>FeO<sub>3</sub>. *Phys. Rev. B* **2021**, *104*, 094109. [[CrossRef](#)]
49. Sarkar, T.; Manna, K.; Elizabeth, S.; Anil Kumar, P.S. Investigation of multiferroicity, spin-phonon coupling, and unusual magnetic ordering close to room temperature in LuMn<sub>0.5</sub>Fe<sub>0.5</sub>O<sub>3</sub>. *J. Appl. Phys.* **2017**, *121*, 084102. [[CrossRef](#)]
50. Schindelin, J.; Arganda-Carreras, I.; Frise, E.; Kaynig, V.; Longair, M.; Pietzsch, T.; Preibisch, S.; Rueden, C.; Saalfeld, S.; Schmid, B.; et al. Fiji: An open-source platform for biological-image analysis. *Nat. Methods* **2012**, *9*, 676–682. [[CrossRef](#)]
51. Singh, M.K. First principle study of crystal growth morphology: An application to crystalline urea. *arXiv* **2006**, arXiv:cond-mat/0602385.
52. Popa, M.; Van Hong, L.; Kakihana, M. Particle morphology characterization and magnetic properties of LaMnO<sub>3+d</sub> perovskites. *Phys. B Condens. Matter* **2003**, *327*, 237–240. [[CrossRef](#)]
53. Bruncková, H.; Medvecký, L.; Ďurišin, J.; Girman, V. Phase transformation and particle morphology of perovskite La<sub>1/3</sub>TaO<sub>3</sub> precursors prepared by polymeric tartrate complex sol–gel method. *Mater. Lett.* **2014**, *115*, 184–186. [[CrossRef](#)]
54. Inkrataite, G.; Kemere, M.; Sarakovskis, A.; Skaudzius, R. Influence of boron on the essential properties for new generation scintillators. *J. Alloy. Compd.* **2021**, *875*, 160002. [[CrossRef](#)]
55. Cho, S.; Yun, C.; Kim, Y.S.; Wang, H.; Jian, J.; Zhang, W.; Huang, J.; Wang, X.; Wang, H.; MacManus-Driscoll, J.L. Strongly enhanced dielectric and energy storage properties in lead-free perovskite titanate thin films by alloying. *Nano Energy* **2018**, *45*, 398–406. [[CrossRef](#)]
56. Kitanaka, Y.; Miyayama, M.; Noguchi, Y. Ferrielectric-mediated morphotropic phase boundaries in Bi-based polar perovskites. *Sci. Rep.* **2019**, *9*, 4087. [[CrossRef](#)]
57. Ibrahim, A.-B.M.A.; Murgan, R.; Rahman, M.K.A.; Osman, J. Morphotropic Phase Boundary in Ferroelectric Materials. In *Ferroelectrics—Physical Effects*; Mickaël, L., Ed.; IntechOpen: Rijeka, Croatia, 2011. [[CrossRef](#)]